Ocean Engineering 343 (2026) 123090

Contents lists available at ScienceDirect

Ocean Engineering

journal homepage: www.elsevier.com/locate/oceaneng

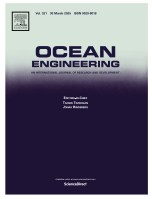

Research paper

A hybrid floating wind-wave energy platform for minimum power baseload

Abel Arredondo-Galeana [a,1,*], Gabriel Thomas Scarlett [b], Maurizio Collu [a], Feargal Brennan [a]

[a] Department of Naval Architecture, Ocean and Marine Engineering, University of Strathclyde, Glasgow, UK
[b] Mocean Energy Ltd, Edinburgh, UK

ARTICLE INFO

Keywords:
Hybrid offshore renewables
Wind power
Wave power
Very large floating platform
Hinged raft WEC

ABSTRACT

We develop a novel hybrid wind-wave energy platform for applications that require a minimum power baseload for continuous operation. The hybrid platform consists of three very large pontoons connected with mechanical hinges. The downstream pontoon carries a 5 MW wind turbine on deck. Wave energy is extracted trough hinge motion. By computing numerically a power matrix for wave energy conversion, and assuming mean power production for the wind turbine, we evaluate the performance of the hybrid platform. Rather than assessing performance in terms of power variability, performance is gauged by determining periods of time when the hybrid platform meets a minimum power threshold, in periods of time of absent wind power. The platform is assessed in three locations with different wind-wave correlation characteristics: One off the coast of Spain, one on the West and one on the East coast of Scotland. It is found that the platform has better performance in locations with high wave power density and low to intermediate wind-wave correlation indices. The hybrid concept, besides being modular and scalable, can meet the requirements of recently considered steady state applications to be deployed offshore. For example, hydrogen electrolysers, which require a minimum power supply for lasting operation.

1. Introduction

Floating offshore wind turbines are expanding to deep water (>100 m) with ever increasing large wind turbines. Nonetheless, deep water operations pose significant cost related challenges for offshore renewable (ORE) technology (Veers et al., 2019). For floating wind, the "modus operandi" consists of one very large wind turbine per floating foundation (Allen et al., 2020; Papi and Bianchini, 2022). This poses significant engineering and cost related challenges to design reliable floating structures that can carry massive wind turbines and can provide platform stability (Arredondo-Galeana and Brennan, 2021; Rodríguez Castillo et al., 2025). Additionally, larger transmission distances combined with the intermittency of wind, produce an increase in dispatch costs, and can incur into associated energy storage costs to satisfy peak demand.

A possible solution to reduce the costs of floating offshore wind, relies in the design of hybrid offshore renewables. Hybrid offshore renewables have the capacity to reduce the levelised cost of energy of offshore wind farms, through reduction of dispatch costs and peak generation requirements (Guo and Ringwood, 2021; Jin and Greaves, 2021; Pennock et al., 2023; Wang et al., 2025). Among the range of options of hybrid renewables, the combination of wind and wave stands out. Several literature reviews have discussed the complementarity and supplementary of both resources from a metocean to a device level perspective (Pérez-Collazo et al., 2015; Wan et al., 2024). Several other studies have focused on site selection metrics and explored synergies for the joint exploitation of wind and wave energy resources. They have done so by examining different regions of the world, for example, the European Atlantic coast (Astariz and Iglesias, 2016), the coasts of Ireland (Fusco et al., 2010), the west Danish coast (Astariz and Iglesias, 2016), the North Sea (Astariz et al., 2018), and further afield, the coast of Australia (Gao et al., 2022; Hosseinzadeh et al., 2025).

Some of the important wind-wave synergy effects that have been identified include: 1) Reduction in power fluctuations and power variability (Fusco et al., 2010; Said et al., 2023). 2) The potential to share installation facilities and thus, reduction of dispatch costs (Pennock et al., 2023). 3) The higher wave energy predictability and mean power density per meter than other forms of offshore renewables, such as solar energy (Reikard et al., 2015; Rusu and Onea, 2017). 4) Suppression of loads or motion in neighboring wind turbine structures (Borg et al., 2013; Astariz et al., 2018; Gaspar et al., 2021; Gubesch et al., 2023). Hence, hybrid or co-located wind and wave systems have emerged as possible candidates to reduce floating ORE costs and improve structural resilience.

* Corresponding author.
E-mail address: abel.arredondo-galeana@strath.ac.uk (A. Arredondo-Galeana).
[1] https://pureportal.strath.ac.uk/en/persons/abel-arredondo-galeana

https://doi.org/10.1016/j.oceaneng.2025.123090
Received 13 May 2025; Received in revised form 30 June 2025; Accepted 5 October 2025

These synergies have driven the development of a plethora of hybrid wind-wave floating concepts across the globe. Most of these concepts have been designed around the most mainstream wind turbine floating structure, the semi-sub (Arredondo-Galeana and Brennan, 2021; Rodríguez Castillo et al., 2025). The predominant use of the semi-sub for hybrid wind-wave platforms is evident in recent state-of-the-art hybrid platform reviews (Dong et al., 2022; Hallak and Guedes Soares, 2025) and in other relevant studies of semi-sub adaptations for wave energy conversion. Specifically, some adaptations involve externally mounted wave energy converters, such as hinged floats (Ghafari et al., 2021; Stansby and Li, 2024), point absorbers (Zhou et al., 2023), or hinged flaps (Celesti et al., 2023), while others focus on internal adaptations incorporating oscillating water columns (Aboutalebi et al., 2024).

In contrast, barge type floating structures for hybrid wind and wave exploitation have been much less considered, despite having a few favourable features. Firstly, barge type floating structures are stable and a competitively economical alternative for floating wind concepts, as demonstrated in Jonkman and Buhl (2007), Ioannou et al. (2020), Edwards et al. (2023). Secondly, the largest demonstrators of hybrid wind-wave platform ever built and tested in the ocean, so far, have been of barge type, through the Poseidon platform of Floating Wind Power (Yde et al., 2014; Edwards et al., 2023). Another industry-led example of hybrid floating platform is the Flex2future concept, which considers relative motion of floaters for wave energy conversion (Flex2Future, 2025).

Thus, in this work, we propose a novel hybrid wind-wave platform that is of the barge-type and is hinged connected. We adopt the concept of a hinged connected very large floating structure used as wind turbine foundation (Zhang et al., 2021). But rather than using the hinges for load alleviation, we utilise hinge motion for wave energy extraction. Stand-alone interconnected floaters have been considered for wave energy extraction. Early mathematical models considered a dual raft type of device (Mei and Newman, 1980), which later evolved to consider multiple connected bodies (Noad and Porter, 2017b,a). Recent years, have seen the study of such devices to include further considerations, such as hydroelasticity effects (Zhang et al., 2018), experimental considerations (Zhang et al., 2023b) and power efficiency absorption (Scarlett et al., 2024). Nonetheless, these studies have focused on wave energy, and to the best knowledge of the authors, have not been considered in combination with wind energy. Note that in extreme events, hinge motion can still be used to alleviate loading of the platform (Zhang et al., 2021; Arredondo-Galeana et al., 2023a). Specifically, the platform consists of a three pontoon barge type floating structure connected with two hinges. A single point low-stiffness mooring line is used upstream of the platform to allow platform passive yaw into the main wave direction. While a 5 MW wind turbine is installed downstream of the platform.

The purpose of the hybrid platform is unique in terms of power supply. Previous works on wind-wave complementarity have focused on reducing variability and providing a smooth power output (Fusco et al., 2010). In this work, we assess the capability of the hybrid platform to provide a minimum power threshold. This requirement stems from offshore applications that had not been considered in the past. For example, the case of hydrogen proton exchange membrane (PEM) electrolysers, whose operational life is reduced when the power baseload drops below 20 % of their rated capacity (Niblett et al., 2024). Hence, new design philosophies and drivers are emerging for wind-wave hybrid platform design, and this work focuses in one of them, which is the ability of the platform to provide a minimum power baseload. Similar to Fusco et al. (2010), we select three different locations with different wind-wave resource correlation. One off the coast of Spain, with a low correlation index, and two off the coast of Scotland, with higher correlation indices.

The main hypothesis of this work is that the platform performs better in the low correlation site, while the main novelties are synthesised as follows:

- The development of a novel hybrid wind-wave floating platform which is modular and scalable.
- Power performance assessment by quantifying the ability of the platform to provide a minimum power baseload, and therefore, reduce wind power downtime.
- Implementation of a numerical model to evaluate platform motion and wave energy performance subject to irregular waves and consider average wind turbine loading.
- Benchmarking of platform numerical model versus available experimental data of a stand alone hinged-connected floating platform.

The structure of the paper is laid out as follows. First, the hybrid platform is introduced. Then, the three proposed locations for the hybrid concept are presented. One with a low wind and wave correlation index off the coast of Spain, and two with higher correlation indices, off the West and East coast of Scotland. Subsequently, the dynamics of the platform are presented. The numerical model of the platform is validated in unloaded conditions and without a wind turbine versus experimental data. Then, the influence of the wind turbine on platform motion is assessed and the power matrix of the platform is quantified. The performance of the hybrid platform is assessed in terms of minimum power threshold and downtime power reduction for the three proposed locations. Metocean data of 20 years (2000–2019) are utilised for the analysis. Lastly, the conclusions of the work are presented.

2. The hybrid platform

In this Section, we introduce the hybrid platform. The platform comprises three pontoons and two hinges, as depicted in Fig. 1. The platform is designed to carry the NREL 5 MW wind turbine. The particulars of the wind turbine are shown in Table 1. Fig. 1 shows that the turbine is supported by the downstream pontoon at the stern of the platform, and wave energy is extracted at the hinge locations. The wind turbine actively yaws into the main wind direction. In this study, we assume that the platform aligns with the predominant wave direction. This assumption is based on the configuration of the platform, which consists of a very large floating platform connected via a single-point mooring line at the bow of the platform, allowing for passive weathervaning. We recognise, however, that in real ocean conditions, the heading of the platform is influenced by multiple factors, including second-order wave drift forces, currents, and wind. As a result, alignment with the wave direction may require considerable time. Future work will therefore include the development of a time-domain model that accounts for heading dynamics. In this proof-of-concept study, we consider the scenario in which the platform is aligned with the main direction of the wave. Accordingly, the rotational axis of the hinges is oriented parallel to the crest of the waves and hinge motion is maximised.

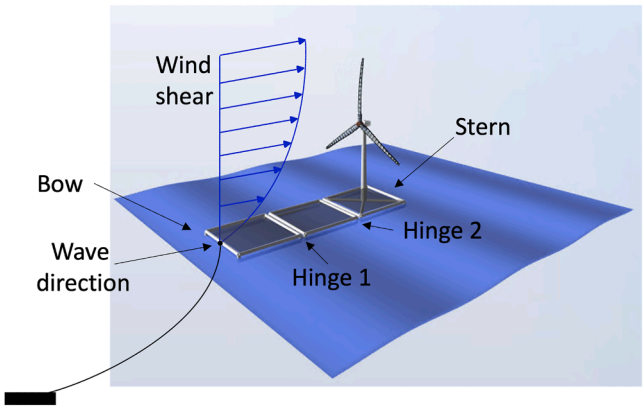

Fig. 1. Three pontoon hybrid platform with turbine mounted downstream of the platform. Wave energy is harnessed through hinge motion. The single point mooring line upstream of the platform allows for passive yaw into the main wave direction.

Table 1
Wind turbine particulars for the 5MW NREL concept (Jonkman et al., 2009).

Wind turbine	Hub height (m)	Rotor width	Rated speed	Cut in speed	Cut out speed	Mass	Rated power
NREL turbine	90 m	126 m	11 m/s	3 m/s	25 m/s	697 tonnes	5 MW

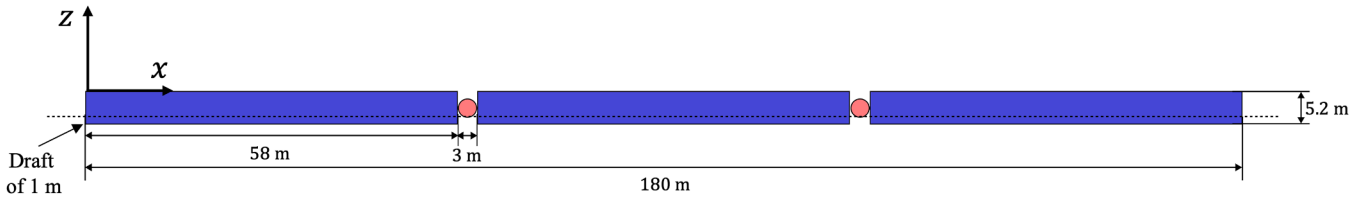

Fig. 2. Schematic of VLFS with global origin, showing length of pontoons (58 m), gap between pontoons (3 m) and the total length of the platform (180 m). The height and draft of the platform are 5.2 m and 1.0 m, respectively.

Table 2
Pontoon specifications of VLFS for this present work, for the ITI energy barge (Jonkman and Buhl, 2007) and the hinged modular raft studied by Zhang et al. (2023b).

Design	Length (m)	Width (m)	Freeboard (m)	Draft (m)	Water displacement (m^3)	Mass (kg)
Present work	58	58	4.2	1.0	3364	3,448,100
ITI energy barge (Jonkman and Buhl, 2007)	40	40	6.0	4.0	6000 (Jonkman and Buhl, 2007)	5,452,000 (Jonkman and Buhl, 2007)
Zhang et al. (2023b)	40	40	10.0	5.0	8000	8,200,000

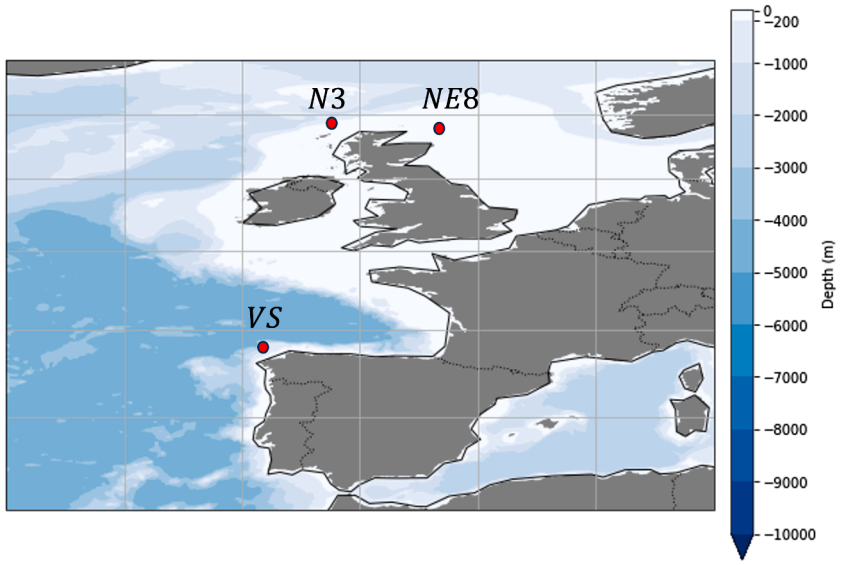

Fig. 3. Selected sites for analysis of hybrid wind wave platform: Villano Sisargas (VS) off the coast of Spain, N3 and NE8, off the west and east coast of Scotland.

By adjusting the draft of the pontoons shown in Fig. 1, and assuming a fixed pontoon surface area, the required buoyancy for the wind turbine and the pontoon can be achieved. Considering water density ρ_g = 1025 kg/m^3, and a very large floating structure (VLFS) pontoon surface area of 58 m × 58 m, a draft of 1.0 m per pontoon is sufficient to provide a buoyancy force $B \approx 5 \times W_t$, where W_t is the weight of the turbine. The water displacement of each pontoon is 3364 m^3. An schematic of the floating platform with main dimensions is shown in Fig. 2. While in Table 2, the dimensions of the pontoons of the platform are compared versus those of the ITI barge (Jonkman and Buhl, 2007) and the pontoons of the hinged raft VLFS design studied in Zhang et al. (2023b). Noteworthy, the ITI barge was a floating platform designed to carry a 5 MW turbine.

The ability of the hybrid platform to resist rolling motion is determined through the width of the platform. Following Zhang et al. (2021), where the rotor plane of the turbine is parallel to the direction of the wave, we compare the moment due to the mean thrust of the turbine and the restoring moment. Considering that for a NREL 5 MW turbine, D = 126 m, a width of $w \approx 0.5D$ limits the rolling angle of the platform to $\phi < 0.5°$. Note that the selection of a small scale wind turbine (≤ 5 MW), facilitates the structural design and allows for ease of transportation and assembly (Arredondo-Galeana and Brennan, 2021).

3. Site selection

Site selection is an important consideration in the performance of a hybrid wind-wave floating platform. Low wind-wave correlation sites could be beneficial to exploit the complementarity of wind and wave power. However, whether this holds true for this novel platform, or whether the performance of the platform subject to intermediate and high correlation sites changes, remain open questions. Hence we consider the three locations depicted in Fig. 3. A swell dominated, low correlation site, off the North West coast of Spain, Villano Sisargas (VS), and higher correlation sites, one off the West coast of Scotland, N3, which is still swell dominated, and one in the North Sea and off the East coast of Scotland, NE8, which is expected to have a higher wind wave correlation due to a shorter fetch. The selection of the sites is restricted to three locations with different wind and wave correlation characteristics,

Table 3
Average wind and wave metocean conditions for NE8, N3 and Villano Sisargas for years 2000–2019 from ESOX database (LAUTEX, 2023).

Location name	Country	Coordinates	α	U_{10}	U_{100}	U_{hub}	H_s	T_p
NE8	Scotland	N 58.25°, W 1.25°	0.0884	8.36	10.25	10.05	1.8425	8.0486
N3	Scotland	N 58.75°, W 6.5°	0.1766	8.64	10.46	10.27	2.6023	10.6302
Villano Sisargas	Spain	N 43.5°, W 9.21°	0.1787	7.73	9.38	9.20	2.4997	10.7493

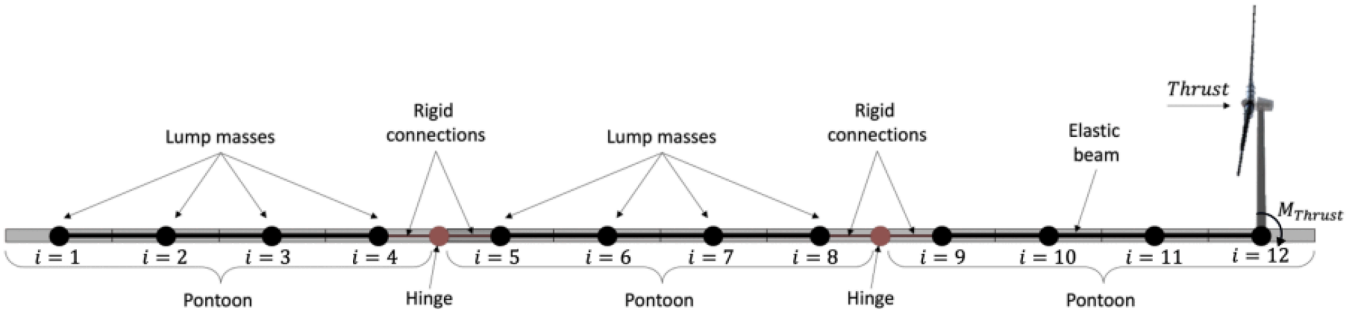

Fig. 4. Discrete beam element model for hinged VLFS with mass and turbine thrust incorporated.

low, intermediate and high correlations, but the methodology to assess the performance of the hybrid platform is applicable to further locations.

The ESOX tool (LAUTEX, 2023), which uses the ERA5 data base, is used to sample the metocean data of the selected locations. The temporal resolution of the ERA5 data base is hourly, while the spatial resolution is 0.25° × 0.25°. In Table 3, the geographical coordinates and the average metocean properties of the locations depicted in Fig. 3 are provided. The metocean properties listed in Table 3 are mainly wind speed at hub height (U_{hub}), significant wave height (H_s) and mean peak period (T_p). To compute U_{hub}, a mean wind speed power law coefficient (α) is computed by considering the mean wind speed at 10 m (U_{10}) and at 100 m (U_{100}). Twenty years of metocean data, ranging from years 2000–2019, are considered to compute the metrics shown in Table 3.

The correlation coefficient can be used as an index of suitable locations for hybrid floating platforms (Astariz and Iglesias, 2017; Kalogeri et al., 2017; Gao et al., 2022), and is defined through the Pearson's correlation such that

$$C(x,y,\tau) = \frac{1}{N}\sum_{i=1}^{N-\tau}\left[\frac{(x_i-\overline{\mu}_x)\cdot(y_{i+\tau}-\overline{\mu}_y)}{\sigma_x\sigma_y}\right], \tag{1}$$

where x and y are the correlation variables, i is the instant in time, τ is the time lag between x and y. In this case, $\tau = 0$, since the wind and wave metocean data sourced from the ERA5 database is sampled with the same origin in time and the same time duration. Then, $\overline{\mu}_x$ and $\overline{\mu}_y$ are the mean of the correlation variables, respectively, σ_x and σ_y are the standard deviation of x and y, respectively, N is the total number of instances in the time series. In this work, the correlation variables used in Eq. (1) are the wave power density of an irregular wave (in deep water) per meter wave crest (W/m), defined as

$$\rho_{wave} = \frac{\rho_s g^2 H_s^2 T_e}{64\pi}, \tag{2}$$

and the wind power density per swept area (W/m^2), defined as

$$\rho_{wind} = \frac{\rho_a U_{hub}^3}{2}. \tag{3}$$

In Eqs. (2) and (3), ρ_s is the water density, g is the gravity of Earth, H_s is the significant wave height, T_e is the wave energy period, ρ_a is the density of air and U_{hub} is the wind speed at hub height. Note that $T_e = 0.9\,T_p$ assuming a JONSWAP spectrum (Arredondo-Galeana et al., 2023b).

To compute the wave energy power (P_{wave}) provided by the hybrid platform, a power matrix considering the effect of irregular waves is developed. Hence, H_S and T_P are used as inputs to the matrix. In the next section, we introduce the hydrodynamic model used to compute the power matrix of the WEC. The power of the turbine (P_{wind}) is assessed through the power curve of the NREL 5MW wind turbine under the assumption that minimal pitching and heave motions do not alter the mean power performance of the turbine (Wen et al., 2018). The assumption of reduced amplitude motions is further assessed in the results section of this manuscript.

4. Numerical model

The numerical model utilised in this work is the frequency domain approach developed for very large floating platforms (VLFS) in Zhang et al. (2018) and applied for hinged connected two-raft system in Zhang et al. (2018). Later, Arredondo-Galeana et al. (2023a) validated the numerical model versus experimental measurements of a rigid and hinged connected VLFS platform constructed with three pontoons. In this work, the numerical model is adapted to include wind turbine loading and the effect of the wave power take-off in a three pontoon, dual-hinge floating system.

Consider Fig. 4, showing three pontoons connected by two mechanical hinges. Each pontoon is discretised into a finite number of segments and each segment is represent by a black lump mass. While the mechanical hinges are denoted with red circles. Each lump mass has 6 degrees of freedom, such that $\boldsymbol{x}_i = [x_i, y_i, z_i, \phi_i, \theta_i, \psi_i]^{\mathrm{T}}$, where x_i, y_i, z_i, ϕ_i, θ_i and ψ_i refer to surge, sway, heave, roll, pitch and yaw, respectively. Index i refers to the i-th lump mass, as depicted in Fig. 4. Consequently, the motion vector of the platform, excluding mechanical hinges, is $\mathbf{X} = [\boldsymbol{x}_1^{\mathrm{T}} \dots \boldsymbol{x}_N^{\mathrm{T}}]^{\mathrm{T}}$, where N is the total number of lump masses.

4.1. Elastic connection

The lump masses are connected to each other with elastic beams with structural stiffness $\boldsymbol{k}$ to account for hydroelastic deformations. The beam connection between two consecutive lump masses, 1 and 2, is depicted in Fig. 5. The 6 degrees of freedom of each lump mass are depicted at the ends of the beam. The global frame of reference $[x_o, y_o, z_o, \phi_i, \theta_o, \psi_o]^{\mathrm{T}}$ is depicted in the Figure.

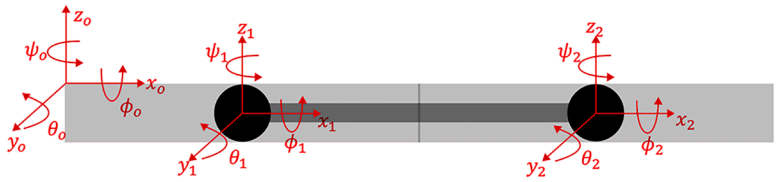

Fig. 5. Elastic beam connection with global and local reference frames for lump mass $i = 1$ and $i = 2$.

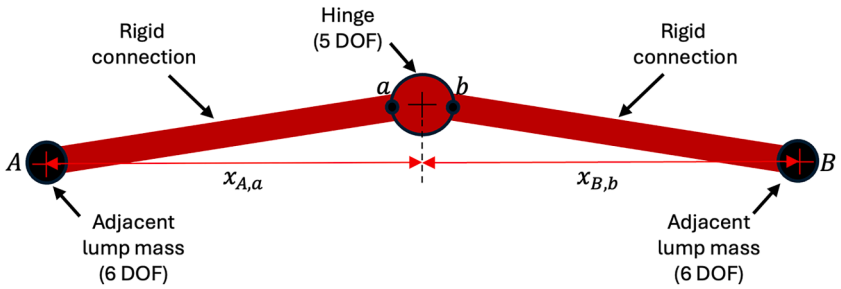

Fig. 6. Hinge connection showing adjacent lump masses A and B adjacent to the hinge, points a and b located at the hinge, and rigid connections between A and a, and between B and b.

The stiffness matrix $\boldsymbol{k}$ of the beam in Fig. 5 is defined as

$$\boldsymbol{k} = \begin{bmatrix}
\frac{EA}{l} & 0 & 0 & 0 & 0 & 0 & -\frac{EA}{l} & 0 & 0 & 0 & 0 & 0 \\
0 & \frac{12EI_z}{l^3} & 0 & 0 & 0 & \frac{6EI_z}{l^2} & 0 & -\frac{12EI_z}{l^3} & 0 & 0 & 0 & \frac{6EI_z}{l^2} \\
0 & 0 & \frac{12EI_y}{l^3} & 0 & -\frac{6EI_y}{l^2} & 0 & 0 & 0 & -\frac{12EI_y}{l^3} & 0 & -\frac{6EI_y}{l^2} & 0 \\
0 & 0 & 0 & \frac{GJ}{l} & 0 & 0 & 0 & 0 & 0 & -\frac{GJ}{l} & 0 & 0 \\
0 & 0 & -\frac{6EI_y}{l^2} & 0 & \frac{4EI_y}{l} & 0 & 0 & 0 & \frac{6EI_y}{l^2} & 0 & \frac{2EI_y}{l} & 0 \\
0 & \frac{6EI_z}{l^2} & 0 & 0 & 0 & \frac{4EI_z}{l} & 0 & -\frac{6EI_z}{l^2} & 0 & 0 & 0 & \frac{2EI_z}{l} \\
-\frac{EA}{l} & 0 & 0 & 0 & 0 & 0 & \frac{EA}{l} & 0 & 0 & 0 & 0 & 0 \\
0 & -\frac{12EI_z}{l^3} & 0 & 0 & 0 & -\frac{6EI_z}{l^2} & 0 & \frac{12EI_z}{l^3} & 0 & 0 & 0 & -\frac{6EI_z}{l^2} \\
0 & 0 & -\frac{12EI_y}{l^3} & 0 & \frac{6EI_y}{l^2} & 0 & 0 & 0 & \frac{12EI_y}{l^3} & 0 & \frac{6EI_y}{l^2} & 0 \\
0 & 0 & 0 & -\frac{GJ}{l} & 0 & 0 & 0 & 0 & 0 & \frac{GJ}{l} & 0 & 0 \\
0 & 0 & -\frac{6EI_y}{l^2} & 0 & \frac{2EI_y}{l} & 0 & 0 & 0 & \frac{6EI_y}{l^2} & 0 & \frac{4EI_y}{l} & 0 \\
0 & \frac{6EI_z}{l^2} & 0 & 0 & 0 & \frac{2EI_z}{l} & 0 & -\frac{6EI_z}{l^2} & 0 & 0 & 0 & \frac{4EI_z}{l}
\end{bmatrix}$$

where I_y and I_z denotes the second moment of area of the cross section with respect to y-axis and z-axis respectively, E refers to the material elastic modulus, G refers to the material shear modulus, l is the length of the element and J is the torsion constant. The structural stiffness matrix of the VLFS ($\mathbf{K_s}$) is obtained by assembling $\boldsymbol{k}$ for consecutive beams connected in series and following standard finite element procedures.

4.2. Hinge connection

In Fig. 4, the connection between hinge and adjacent lump masses is a rigid connection. Hence, when assembling the VLFS structural matrix $\mathbf{K_s}$, no elastic beam is modelled adjacent to the hinge. Consider the hinge depicted in Fig. 6. The hinge is connected to lump masses A and B through rigid connectors. Two points on the hinge, a and b, are situated on the hinge itself, on the left and right sides, respectively. Lump masses A and B have 6 degrees of freedom, i.e, $\boldsymbol{x}_A = [x_A, y_A, z_A, \phi_A, \theta_A, \psi_A]^{\mathrm{T}}$ and $\boldsymbol{x}_B = [x_B, y_B, z_B, \phi_B, \theta_B, \psi_B]^{\mathrm{T}}$. While a and b have 5 degrees of freedom, because the hinge rotates around the hinge axis and eliminates pitch, i.e, $\boldsymbol{x}_a = [x_a, y_a, z_a, \phi_a, \psi_a]^{\mathrm{T}}$ and $\boldsymbol{x}_b = [x_b, y_b, z_b, \phi_b, \psi_b]^{\mathrm{T}}$.

Because a and b are both located at the hinge, then

$$\boldsymbol{x}_a - \boldsymbol{x}_b = 0. \tag{4}$$

Then, $\boldsymbol{x}_{\mathrm{a}}$ and $\boldsymbol{x}_{\mathrm{b}}$ can be computed from rigid body dynamics, such that

$$\boldsymbol{x}_a = \mathbf{L}_a \boldsymbol{x}_A \quad \text{and} \quad \boldsymbol{x}_b = \mathbf{L}_b \boldsymbol{x}_B, \tag{5}$$

where A and B are the adjacent lump masses to the hinge, $\mathbf{L}_a$ and $\mathbf{L}_b$ are the rigid-body Lagrangian motion transformation matrices between lump masses A and B, to points a and b, respectively. Following Zhang et al. (2021), the Lagrangian transformation matrices are simplified to

$$\mathbf{L}_a = \begin{bmatrix} 1 & 0 & 0 & 0 & 0 & 0 \\ 0 & 1 & 0 & 0 & 0 & x_{A,a} \\ 0 & 0 & 1 & 0 & -x_{A,a} & 0 \\ 0 & 0 & 0 & 1 & 0 & 0 \\ 0 & 0 & 0 & 0 & 0 & 1 \end{bmatrix} \quad \text{and}$$

$$\mathbf{L}_b = \begin{bmatrix} 1 & 0 & 0 & 0 & 0 & 0 \\ 0 & 1 & 0 & 0 & 0 & -x_{B,b} \\ 0 & 0 & 1 & 0 & x_{B,b} & 0 \\ 0 & 0 & 0 & 1 & 0 & 0 \\ 0 & 0 & 0 & 0 & 0 & 1 \end{bmatrix}, \tag{6}$$

where $x_{A,a}$ and $x_{B,b}$ are the distances between A to a and B to b, respectively.

The motion vectors of the adjacent lump masses, $\boldsymbol{x}_A$ and $\boldsymbol{x}_B$, are part of motion vector $\mathbf{X}$. In contrast, the motion vectors of the non-adjacent lump masses do not influence the motion of the hinge. Then, combining Eq. (5), into Eq. (4), we can write

$$\boldsymbol{\Xi}\,\mathbf{X} = [\mathbf{0}_1 \;\; \mathbf{L}_a \;\; -\mathbf{L}_b \;\; \mathbf{0}_2]\,\mathbf{X} = \mathbf{0}, \tag{7}$$

where $\boldsymbol{\Xi}$ is the motion constraint matrix, and where $\mathbf{0_1}$ and $\mathbf{0_2}$ are zero matrices of dimensions $5 \times 6 \times N_l - 1$ and $5 \times 6 \times N_r - 1$, respectively. Here, N_l and N_r are the total number of lump masses to the left and right of the hinge, respectively. The hydrodynamic model assumes point loads acting on the lump masses to represent the distributed hydrodynamic loads that are, in reality, exerted in each module. Consequently, the point load that acts on the hinge is translated to the adjacent lump masses, such that

$$\mathbf{F}_J^{new} = \boldsymbol{\Xi}^{\mathbf{T}} \mathbf{F}_J, \tag{8}$$

where $\mathbf{F}_J$ is the force on the hinge of dimensions 5×1 and $\boldsymbol{\Xi}^T$ is the transpose of $\boldsymbol{\Xi}$.

4.3. Balance of hydrodynamic forces

For the platform depicted in Fig. 4, the balance of forces and the influence of the two hinges in the motion response of the platform is

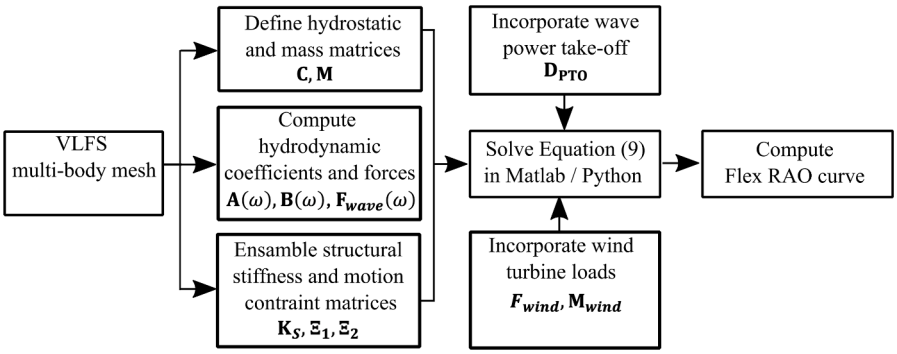

Fig. 7. Flow chart to solve hydrodynamic problem stated in Eq. (9).

given by:

$$\begin{bmatrix} -\omega^2(\mathbf{M}+\mathbf{A}(\omega)) - i\omega(\mathbf{B}(\omega)+\mathbf{D}_{\text{PTO}}) + \mathbf{C} + \mathbf{K}_S & \Xi_1^T & \Xi_2^T \\ \Xi_1 & \mathbf{0} & \mathbf{0} \\ \Xi_2 & \mathbf{0} & \mathbf{0} \end{bmatrix} \begin{bmatrix} \mathbf{X} \\ \mathbf{F}_1 \\ \mathbf{F}_2 \end{bmatrix} = \begin{bmatrix} \mathbf{F}_{wave} + \mathbf{F}_{wind} \\ \mathbf{0} \\ \mathbf{0} \end{bmatrix}, \tag{9}$$

where the first line of the system of Eq. (9) shows the balance of external forces applied to the hybrid platform, where $\mathbf{M}$ is the mass, $\mathbf{A}(\omega)$ is the added mass, $\mathbf{B}(\omega)$ is the radiation damping, $\mathbf{D}_{\text{PTO}}$ is the power take off damping, which constitutes a force that is proportional to the velocity $i\omega\mathbf{X}$ (Folley and Whittaker, 2010), $\mathbf{C}$ is the restoring matrix, $\mathbf{K}_S$ is the structural stiffness matrix to account for elastic effects of the platform (Arredondo-Galeana et al., 2023a; Zhang et al., 2023a), $\Xi_1^{\mathbf{T}}\mathbf{F}_1$ and $\Xi_2^{\mathbf{T}}\mathbf{F}_2$, are the forces at the two hinges translated to the adjacent lump masses of the hinge (Arredondo-Galeana et al., 2023a; Zhang et al., 2023a), $\mathbf{F}_{wave}$ is the wave excitation force and $\mathbf{F}_{wind}$ is the wind loading in the frequency domain. The second and third equations $\Xi_1\mathbf{X} = 0$ and $\Xi_2\mathbf{X} = 0$, shown in Eq. (9), respectively, arise because the spatial location of the hinges, is the same, when determined either from the left or the right adjacent lump masses.

Viscous losses are not considered in Eq. (9), since previous studies where the pontoon length is significantly greater than the draft have shown that potential flow model assumptions are sufficiently accurate to predict the motion response of hinged connected structures (Arredondo-Galeana et al., 2023a). Additionally, for low mooring line stiffness, numerical models that include a consideration for mooring line forces yield similar results to models that do not consider them (Chen et al., 2023). Hence, in this work, mooring line forces are not considered, since the mooring line is of low stiffness to allow for pitch and heave motions of the platform.

Wind turbine loads in the hybrid platform are accounted for by incorporating the mass and the inertia of the monopile and rotor-nacelle-assemble (RNA), to the lump mass where the wind turbine is mounted. The mean wind turbine thrust is applied as a constant moment at the base of the platform where the wind turbine is installed. The external wind turbine load is denoted as $\mathbf{F}_{wind}$ in Eq. (9). A constant moment is considered for wind turbine loading under the assumption that the mean loads do not change when the pitching motions of the turbine are maintained below 10° (Wen et al., 2018). This assumption is discussed in the Results section of the manuscript.

4.4. Solution of problem

The added mass $\mathbf{A}(\omega)$, radiation damping $\mathbf{B}(\omega)$, coefficients, and Froude-Krylov forces ($\mathbf{F}_{wave}$) in Eq. (9) were computed using a multi-body approach in Hydrostar, consistent with the methodology presented in this paper. The specific Hydrostar data and setup was originally developed for Arredondo-Galeana et al. (2023a). The hydrodynamic data ($\mathbf{A}(\omega)$, $\mathbf{B}(\omega)$ and $\mathbf{F}_{wave}$) have been reutilised in the present work and appropriate credit is provided in the Acknowledgements section. In the setup, the full-scale platform is segmented into $N = 12$ bodies. Each body is meshed with 200 panels. A small gap of 0.01 m is left between each body. A range of full-scale frequencies from 0.25 rad/s to 0.88 rad/s, in increments of 0.063 rad/s, is generated. This corresponds to model-scale frequencies from 0.4 Hz to 1.4 Hz, in steps of 0.1 Hz, based on a 1:100 model scale. The shape of the matrices is $6N \times 6N$ for $\mathbf{A}(\omega)$ and $\mathbf{B}(\omega)$, and $6N \times 1N$ for the $\mathbf{F}_{wave}$ vector. Each N-th segment of the platform has a corresponding mass $\mathbf{M}$ and hydrostatic $\mathbf{C}$ matrix that depend on the dimensions of the body (Zhang et al., 2021). The size of $\mathbf{C}$ and $\mathbf{M}$ is also $6N \times 6N$. Eq. (9) is solved in software Matlab by incorporating the stiffness matrix $\mathbf{K}_S$, motion constrain matrices Ξ_1 and Ξ_2, the power take-off damping $\mathbf{D}_{\text{PTO}}$ and the wind force vector $\mathbf{F}_{wind}$. Note that $\mathbf{F}_{wind}$ is installed in the $N = 10$ element of the platform. The flow chart of in Fig. 7 summarises the solution procedure.

4.5. Wave energy conversion

From the solution of Eq. (9), we focus on the heave (Δz) and pitch ($\Delta\theta$) components of the motion vector $\mathbf{X}$. The relative pitch of the hinge, hereafter referred to as flex of the hinge ($\Delta\theta$) is defined as

$$\Delta\theta = \theta_1 - \theta_2, \tag{10}$$

where θ_1 and θ_2 are the pitch angles computed for the left and right pontoons to the hinge. In this case, we consider the numerically computed pitch of the left and right adjacent lump masses to the hinge. The mean power captured by the hinge, in the frequency domain is defined as

$$\overline{P} = \frac{1}{2}\omega^2 d_{\text{PTO}}|\Delta\theta|^2, \tag{11}$$

where ω is angular frequency of the hinge, d_{PTO} is the damping coefficient, where following Zhang et al. (2018), is applied to the pitching motion degree of freedom of the adjacent lump masses to the hinge, and where $\Delta\theta$ is the flex angle of the hinge in radians per meter wave height. Later in the manuscript, the optimum numerical value for d_{PTO} is computed.

To consider the influence of irregular waves, a wave amplitude spectrum, $S(\omega)$, is discretised in the frequency domain and used to generate individual waves of wave amplitude A_j, where j, in this case, is the index denoting the individual wave. The amplitude of the discrete wave components is given by

$$A_j = \sqrt{2S(\omega_j)\Delta\omega}, \tag{12}$$

where $S(\omega_j)$ is the amplitude of the spectrum at the j-th frequency ω_j, and $\Delta\omega$ is the discretisation step of the spectrum. Similar to the irregular wave analysis carried out in Arredondo-Galeana et al. (2024) for a wave energy converter, we utilise the definition of the JONSWAP spectrum provided by the DNV Environmental Conditions And Environmental Loads Practice Manual (DNV, 2007). Then, the average power for a given sea state is computed as

$$P = \sum_j^N \overline{P}_j A_j^2, \tag{13}$$

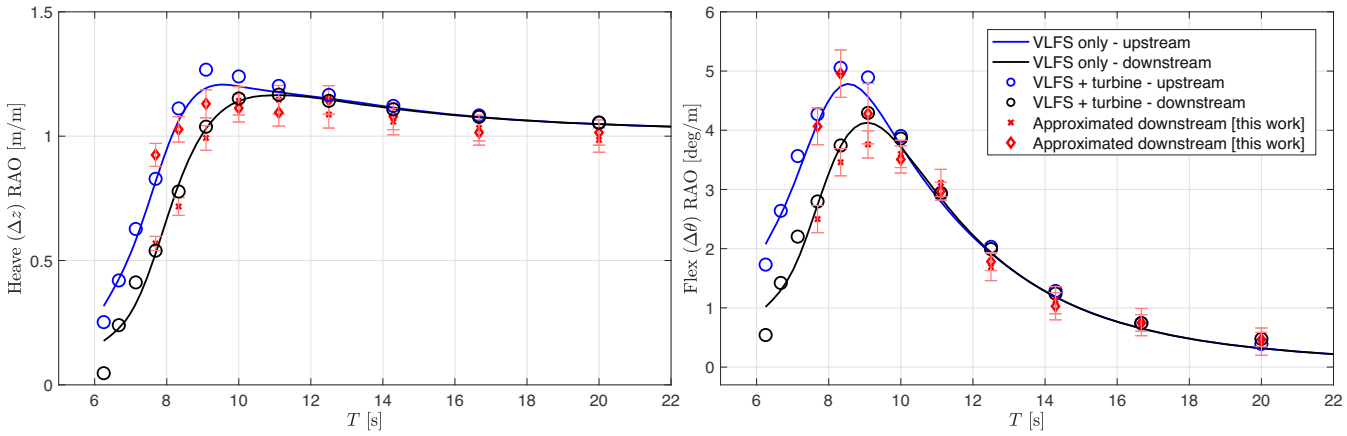

Fig. 8. a) Heave (Δz) and b) flex ($\Delta\theta$) RAO curves for hinged VLFS only and hinged VLFS with wind turbine. Results are computed by considering an underdamped response and comparing VLFS only curve to RAO data measured in downstream pontoon (Arredondo-Galeana and Brennan, 2021).

where j indicates the j-th frequency and N is the total number of frequencies in which the JONSWAP spectrum is discretised, $\overline{P}_j$ is the average power of the j-th frequency computed with Eq. (11) and A_j is the j-th wave amplitude computed with Eq. (12).

5. Results

Platform dynamics

As an initial step in platform motion analysis, we consider the response of the hinged connected very large floating platform only, referred in this Section as VLFS, without wind turbine loading, and assuming an underdamped response, i.e. unloaded hinge (McNatt and Retzler, 2020). The response amplitude operator (RAO) curves for heave (Δz) and flex ($\Delta\theta$) of the upstream and downstream hinges are plotted in Fig. 8a and b, respectively. Both Δz and $\Delta\theta$ are normalised by wave amplitude and plotted as a function of the wave period. In both Fig. 8a and b, the Δz and $\Delta\theta$ of the "VLFS only" case are plotted with blue solid lines for the upstream hinge, and with black solid lines for the downstream hinge.

Subsequently, we include wind turbine loading in the platform and refer to this case as "VLFS + turbine". Results for Δz and $\Delta\theta$ are plotted with circular scattered markers in both Fig. 8a and b, respectively. The color notation is consistent with the VLFS only case, and blue markers are used for the upstream hinge, and black markers are used for the downstream hinge in both of the figures.

In Fig. 8a, Δz of the upstream and downstream hinge are compared versus experimental data measured at the Kelvin Hydrodynamics Laboratory (KHL) at the University of Strathclyde in a hinged-connected VLFS prototype. In the tests, no turbine and no power take-off mechanism at the hinges were included. Further details of the experimental setup are available in Arredondo-Galeana and Brennan (2021) and the data with a video showing the experimental setup are available in a Zenodo open-access repository (ARREDONDO-GALEANA, 2023). The experimental error in Δz was estimated to be approximately 5 % and is depicted with the error bars in Fig. 8a.

For the downstream hinge, where motion between pontoons is typically symmetric for all tested wave periods (ARREDONDO-GALEANA, 2023), an approximation of $\Delta\theta$ was derived from heave measurements. In the experiment, four heaving measuring points were available in each pontoon (Arredondo-Galeana et al., 2023a), one close to the hinge and the others at increasingly further distance. The instance of maximum Δz at the point closest to the hinge was used to sample the Δz of the rest of the heave measurement points along the same pontoon. With a total of four heave measurements available per pontoon, three flex angle estimations were computed for every T sampled experimentally in Fig. 8a, i.e. 9 wave periods. The optimal path that minimised the total flex angle squared difference between consecutive periods, while retaining the peak response, was found. A constraint was imposed such that the flex angle at $T = 25$ s was 0°. This is a known condition, since at very long wave periods ($T \geq 25$ s), the three pontoons ride the wave, and no hinge motion occurs (Arredondo-Galeana et al., 2023a). Lastly, adjacent averaging was applied around the peak value.

For the upstream hinge, where the motion between pontoons is asymmetric at low periods ($T < 10$ s), the experimental $\Delta\theta$ is computed based on the downstream hinge $\Delta\theta$ approximation and the percentage change observed in Δz between upstream and downstream hinges. Hence, the error between upstream and downstream $\Delta\theta$ is considered the same.

The experimental uncertainty in the flex estimation was calculated using the pooled standard deviation, which combines the variances of the three repeated flex measurements across the tested periods to provide a robust estimate of measurement variability. The flex and uncertainties computations were made for the downstream hinge and are included as supplementary material. The pooled standard deviation was 0.27 deg/m and is plotted as error bars in Fig. 8b. The resulting uncertainties ranged from 62 % to 24 % for long wave periods ($T \geq 14$ s), due to low heave displacements and pitch angles, and with an average uncertainty of 10 % across shorter wave periods ($T < 14$ s), where heave motion mas more prominent and pitch angles were greater than 1°. To further reduce uncertainty in flex angle estimation, wave amplitude measurements of 20 mm were used to maximise physical heave displacement and minimise the relative error in pitch angle estimation. For consistency and normalisation, heave values were scaled to correspond to a 10 mm wave amplitude when computing pitch angles. Therefore, results in Fig. 8b are presented in degrees per meter (deg/m), assuming a 1:100 scale model, equivalent to a full-scale platform encountering 1 m wave heights.

Fig. 8a shows that when $T > 10$ s, the heave responses of the upstream and downstream hinge have a similar behavior. As T grows, i.e. $T \geq 20$ s, $\Delta z \approx 1$. This asymptotic condition is characteristic, when the wave wavelength is significancy longer than the length of the full platform (Arredondo-Galeana et al., 2023a). In contrast, when $T \leq 10$ s, the heave response of the upper hinge is higher than the response of the downstream hinge. This is because, at higher frequencies, i.e. shorter wavelengths, the upstream hinge absorbs most of the energy, attenuating the wave downstream. Figure 8a shows that in terms of heave response, the influence of the turbine is almost negligible, and therefore, most of the heave dynamics of the platform are governed by hydrodynamic loading.

Regarding hinge flex motion, Fig. 8b shows that the upstream and downstream hinge have a similar behavior also when $T > 10$ s. In contrast, for shorter waves, i.e. $T \leq 10$ s, the upstream hinge has a more

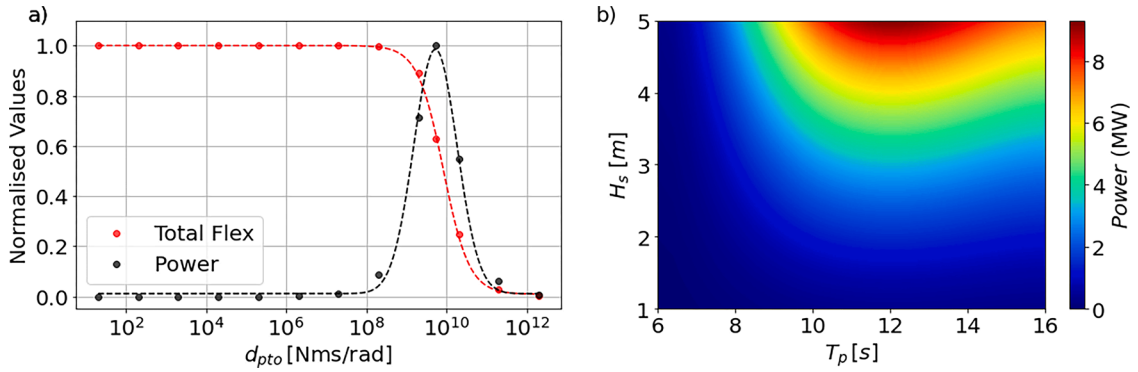

Fig. 9. a) Normalised total flex and power versus different values of power take-off damping (d_{PTO}) and b) wave power matrix of hybrid platform. Considering $d_{\mathrm{PTO}} = 5.5\,\mathrm{GNms/rad}$.

pronounced response. Furthermore, Fig. 8b shows that the flex resonant frequency of the upstream hinge occurs at about $T \approx 8.5$ s, whilst for the downstream hinge the resonant peak occurs at $T \approx 9.5$ s. At the resonant peaks, the highest flex angle at the upstream hinge is close to 5°/m. In contrast, the highest flex angle of the downstream hinge is close to 4°/m. Noteworthy, the influence of the wind turbine, denoted by the circular markers in Fig. 8b, show a negligible effect also in the flex angle of the platform.

Two critical performance factors stand out from Fig. 8b. Firstly, it can be seen that the peak flex response of the upstream and downstream hinges lie over the range of $8\,\mathrm{s} \leq T \leq 10$ s. This range of periods typically coincides with peak periods of high probability sea states in the European Atlantic Coast (Arredondo-Galeana et al., 2023b, 2024). Secondly, because the upstream hinge absorbs more wave energy and imposes higher flex angles than the downstream hinge, then the optimum position of the wind turbine, in terms of motion disturbance is the downstream pontoon. Furthermore, we recall that the results presented here are for an underdamped response. Additional control strategies, such as overdamped and optimal PTO damping (Scarlett et al., 2024), can be implemented to maximise power extraction in the upstream hinge, and mitigating further the motion of the downstream hinge.

With respect to wind turbine power performance, it has been demonstrated that for a low range of pitch amplitude motions, the mean power performance of the turbine remains relatively stable (Tran and Kim, 2015; Wen et al., 2018). Hence, because in general, the pitch angle of the downstream pontoon is the lowest, and remains typically below or circa to 10°, then the range of motion shown in Fig. 8b confirms that a constant power performance for the wind turbine can be considered. In particular, the turbine is also equipped with power control capabilities to provide a stable power output above rated speed (Wen et al., 2018). Therefore, we consider the mean curve power of the NREL 5 MW turbine to compute the power production of the turbine.

Wave power performance

To assess wave energy performance of the hybrid platform, we perform a sweep of different d_{PTO} values at three different wave frequencies (0.3 Hz, 0.5 Hz and 1.0 Hz) to find out the optimum d_{PTO} value for wave power production. Fig. 9a shows the normalised total flex angle of the platform and the normalised mean power computed with Eq. (11) versus d_{PTO}. For clarity, only the case of 0.5 Hz is presented in Fig. 9a, although the rest of the cases (0.3 Hz and 1.0 Hz) show similar performance. It can be seen in Fig. 9a, that as $d_{\mathrm{PTO}} \geq 1\,\mathrm{GNms/rad}$, the total flex starts to decrease. In contrast, the normalised power increases, reaching its maximum level at $d_{\mathrm{PTO}} = 5.5\,\mathrm{GNms/rad}$. At this optimum d_{PTO}, the total flex drops to about 62 % of the underdamped response. Hence, for the remaining of our study, the optimum d_{PTO} is selected as operating point of the hybrid platform.

The power matrix of the hybrid platform is computed for a total of 30 sea states. The sea states corresponded to the combination of significant peak periods (T_p) and significant wave heights (H_s) over the range of 6 s to 16 s in increments of 2 s, and over the range of 1 m to 5 m in increments of 1 m, respectively. This range of sea states covers the majority of significant wave height (H_s) and peak period (T_p) occurrences over the 20-year metocean dataset from the ERA5 database. Specifically, it captures 95 % of H_s and 98 % of T_p for VS, 95 % of H_s and 98 % of T_p for N3, and 99 % of both H_s and T_p for NE8.

The power per sea state is computed with Eq. (13) and results are interpolated to a finer grid of 50 × 50 elements. A grid sensitivity analysis was performed by evaluating grid sizes of 10 × 10, 25 × 25, 50 × 50 and 100 × 100. The results showed that power computations based on metocean data converged after the 50 × 50 power matrix. Thus, this grid size was selected to balance computational efficiency and accuracy. The matrix is computed assuming optimal damping and average turbine loading on the platform. Results are presented in Fig. 9b.

The power matrix shown in Fig. 9b highlights that the wave energy subsystem of the hybrid platform has a broad band response, with the highest values extending over the range of 10 s to 14 s, with a local maximum at $H_s = 5\,\mathrm{m}$ and at $T_p = 12\,\mathrm{s}$. The broad band response shown in the power matrix is associated to the combined effect of the two hinges. Additionally, damping flattens the RAO curve and shifts the peak response to the right hand side of the peaks detected in Fig. 8b, which were located originally between $8\mathrm{s} < T < 10\,\mathrm{s}$. Lastly, larger T_p sea states contain more energy (see Eq. (13)). This also contributes to the maximum response of the power matrix shown in Fig. 9b to be detected at $T_p = 12\,\mathrm{s}$, and to the right hand side of the peaks identified in Fig. 8b. Note that the shape of the power matrix coincides with related studies on wave energy generation through floating platforms composed by hinged elastic plates (Tay, 2019).

We recall that one of the main aims of this paper is to assess the performance of the hybrid platform in sites with different metocean properties, i.e. swell dominated sites versus wind-wave dominated sites (see Fig. 3). Therefore in the next section, we characterise N3, NE8 and VS, in terms of wave and wind power densities (Eqs. (2) and (3)) and in terms of wind and wave correlation index (Eq. (1)). Subsequently, we utilise the power matrix computed in Fig. 9b, and the power curve of the NREL 5 MW wind turbine to assess the performance of the hybrid platform to provide a minimum power threshold and reduce wind power downtime. Note that the power curve of the NREL 5 MW wind turbine was computed in software ASHES (Thomassen et al., 2012).

Power density correlation of sites

An important aspect that will affect the performance of the hybrid platform is the availability of wind and wave power. Hence, the monthly wind and power density averaged over 20 years (2000–2019) are shown in Fig. 10a and b, respectively. Results are shown for the three selected

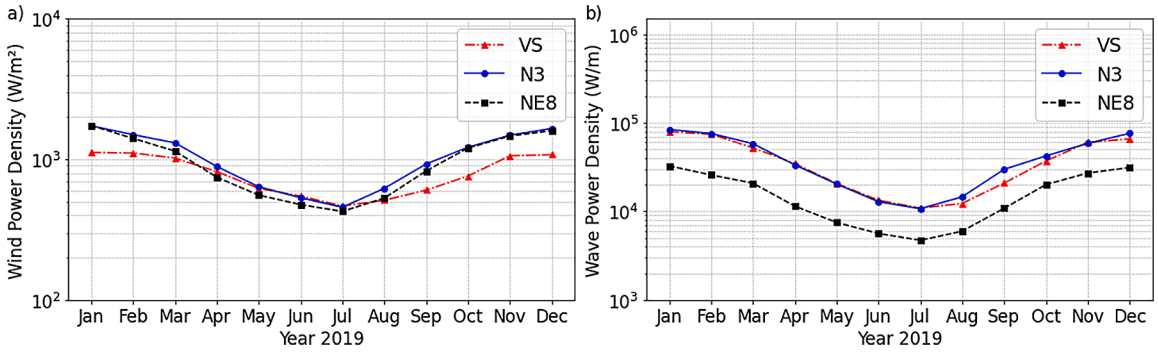

Fig. 10. Monthly average a) wind and b) wave power densities for VS, N3 and NE8 averaged over 20 years from 2000 to 2019.

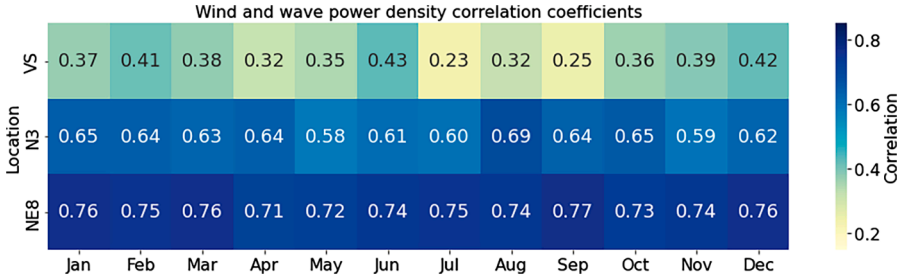

Fig. 11. Monthly average wind and wave power density correlation coefficients, averaged over 20 years (2000–2019), for VS, N3 and NE8.

sites, VS, N3 and NE8 with red, blue and black marker lines, respectively. Note that the monthly wind and wave power densities are computed by averaging the hourly data of U_{hub}, H_s and T_p and by using Eqs. (3) and (2), respectively

It can be seen that both Fig. 10a and b show a bathtub shape where the highest power density is available in the winter months from November to February, and the lowest power density is available in the summer months from May to August. Noteworthy, the wind power density is similar for the three locations in Fig. 10a, with a slight drop towards the edges in VS. In contrast, Fig. 10b shows that the wave power density is lowest in NE8 throughout the full year, as opposed to the wave power density of open sea locations such as N3 and VS. This could be a determining factor in the performance of the hybrid platform.

Prior to analysing the performance of the hybrid platform, and as a subsequent step in site characterisation, we now look at the correlation between wind and wave in N3, NE8 and VS. The monthly average wind and wave power correlation coefficients are presented in Fig. 11, where the vertical axis shows VS, N3 and NE8 from top to bottom, and the horizontal axis shows the monthly coefficients averaged over 20 years (2000–2019). Hourly data and Eqs. (1)–(3) are used to compute the monthly average correlation coefficients. The colorbar of Fig. 11 shows the color code for the correlation coefficient, where a high value corresponds to dark blue ($C > 0.7$), and a low correlation value corresponds to light yellow ($C < 0.4$).

Fig. 11 confirms that throughout the year, VS off the coast of Spain has the lowest correlation coefficients, with a yearly average value of 0.35, compared to 0.63 and 0.75 for N3 and NE8, respectively. The locations selected off the coast of Scotland have clearly higher correlation coefficients than those in VS. NE8, in the North Sea, has higher correlation coefficients than N3, possibly because N3 is exposed to the Atlantic Ocean (see Fig. 3), where swell waves might still be present, as in the case of VS. In contrast, NE8 is located in the North Sea and surrounded by continental masses. Therefore, sea states do not fully develop as in the open ocean, and waves are directly related to local wind.

In the following Section, we investigate whether the performance of the hybrid platform is superior in low correlation sites, such as VS, or whether the availability of power is more important to the performance of the hybrid platform.

Hybrid platform assessment

We investigate the performance of the hybrid platform in the three different locations depicted in Fig. 3. The locations are: Villano-Sisargas (VS) off the coast of Spain, N3 off the West, and NE8 off the East coasts of Scotland. We recall that VS, N3 and NE8 have low, intermediate and high wind wave correlation indices, respectively, as indicated in Fig. 11.

As performance metric, the power downtime of wind turbine versus hybrid platform is compared. Power downtime in the hybrid platform is considered when wave power drops below a certain power threshold, in periods of absent wind power. For the case of the hybrid platform, we consider 1 MW wave power (20 % rated power of 1 PEM electrolyser rated at 5 MW - the same rating as the wind turbine), as the power production threshold. In contrast, for the case when only the wind turbine operates, power downtime is considered when the wind speed at hub height is below or above the rated cut-in or cut-out speeds, respectively, i.e. when the turbine does not produce power. Monthly power downtime averaged over 20 years (2000–2019) is computed for the twelve months of a year, assuming operation of the wind turbine only, and operation of the hybrid platform, with wind and wave power.

Power downtime is plotted as fraction percentage time during each month in the polar plots of Fig. 12a–c, for VS, N3 and NE8, respectively. In the figures, wind power downtime is delimited with dotted lines and highlighted with lightly shaded colours. While, wind-wave power downtime areas are delimited with solid lines and darkly shaded colours. Red, blue and black colours are used for VS, N3 and NE8, respectively.

The polar plots of Fig. 12 show that power downtime increases during the summer months and decreases towards the winter months in the three locations. This behaviour is associated to the seasonal availability of the resources shown in Fig. 10.

In terms of wind power downtime, the polar plots show that the wind power downtime is higher in VS (Fig. 12a), followed by NE8 (Fig. 12c) and then by N3 (Fig. 12b). The yearly downtime averages are 7.4 %, 5.4 % and 4.7 % for VS, NE8 and N3, respectively. To understand these patterns, it is necessary to average the monthly wind power density values shown in Fig. 10a. Wind power density values for VS, NE8 and N3 are 0.81×10^3 W/m^2, 1.01×10^3 W/m^2 and 1.08×10^3 W/m^2, respectively. Hence, the higher the wind power density of a site, the lower the associated wind power downtime.

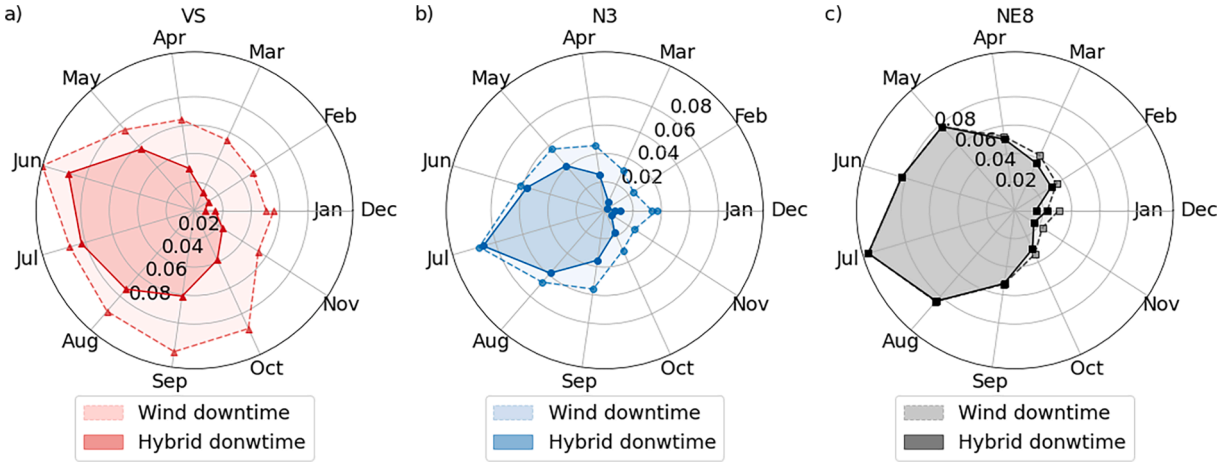

Fig. 12. Monthly average wind power downtime limited with dotted lines and lightly shaded colors versus hybrid power downtime limited by solid lines and darkly shaded colors during a 20 year period (2000–2019) for a) VS, b) N3 and c) NE8.

In terms of hybrid power performance, the polar plots show that power downtime reduction is the highest in VS (Fig. 12a), followed by N3 (Fig. 12b), and very minimal for NE8 (Fig. 12c). Specifically, the highest power downtime reduction between wind turbine and hybrid platform case occurs in VS, with an average yearly reduction from 7.4 % downtime to 4.2 % downtime. For N3, the yearly power downtime reduction goes from 4.7 % to 3.0 %. Lastly, for NE8, the yearly power downtime drops from 5.4 % to 5.1 %.

The power downtime performance of the hybrid platform is dependent on the performance of the wave energy converter and on the selection of wave power threshold. However, wave power density and wind and wave correlation indices are determining factors as well. By averaging the monthly wave power density values shown in Fig. 10b, we obtain $\rho_{wave} = 3.96 \times 10^5$ W/m, $\rho_{wave} = 4.24 \times 10^5$ W/m and $\rho_{wave} = 1.67 \times 10^5$ W/m for VS, N3 and NE8, respectively. While the yearly averaged wind and wave correlation indices are 0.35, 0.63 and 0.78 for VS, N3 and NE8, respectively. Hence, the location with one of the highest yearly ρ_{wave} and with the lowest yearly correlation index, VS, shows the highest average percentage drop in power downtime with a drop of 43 % when the hybrid platform is in operation. In second place, N3, with the highest yearly ρ_{wave} and intermediate correlation index, shows an intermediate drop in performance with a drop of 36 %. In last place, NE8, shows a drop of only 6 %, because of the lowest ρ_{wave} and highest correlation index.

These results suggest that the hybrid platform is more effective in reducing power downtime in locations with high wave power density and with low or intermediate wind and wave correlation indices, such as VS and N3, which are swell dominated regions facing the European Atlantic Coast, as depicted in Fig. 3.

The power downtime, correlation index and power density computations were carried out locally on a standard modern laptop. Specifically, a MacBook Pro-equipped with an M1 Max chip, with 10 CPU cores and 64 GB of RAM, was used. MATLAB was used to solve the dynamics of the platform and to perform the site specific and power performance computations, while Python was used to compute the wave power performance analysis, including power take-off damping curve and wave power matrix of Fig. 9.

With this hardware and software setup, the computational time required to quantify the monthly hybrid and wind power downtime, correlation index and power density metrics over 20 years of metocean data, with hourly resolution, was approximately 40 seconds. For a full year of analysis, this was equivalent to 8 minutes per location.

For the wave power matrix, the power per sea state, which included 100 discrete waves, was computed in 0.02 seconds. Regarding the dynamics of the platform, we recall that the hydrodynamic coefficient computations were adopted from Arredondo-Galeana et al. (2023a). Therefore, the main computational task was solving Eq. (9) to compute the RAO plots shown in Fig. 8. The solution of Eq. (9) was achieved in approximately 0.4 seconds per tested frequency.

Sensitivity analysis

The previous sections considered 1 MW, as the criterion to determine whether wave power was available in the hybrid platform, and therefore, whether wind power downtime reduction occurred. Nonetheless,

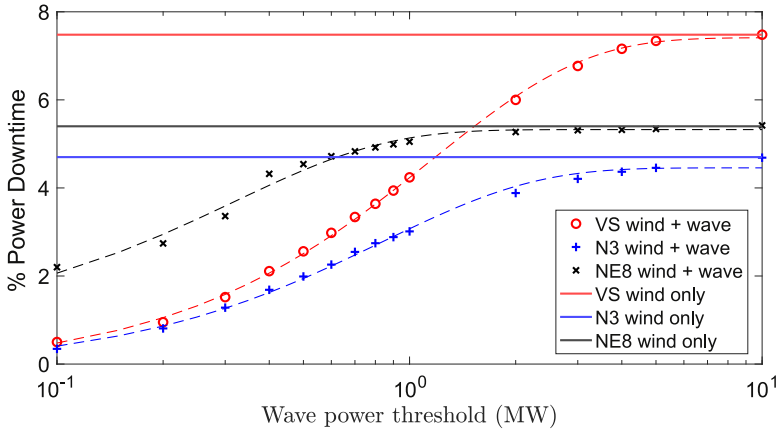

Fig. 13. Sensitivity analysis of hybrid downtime power versus different wave power thresholds computed with metocean data during 20 years (2000–2019) for VS, N3 and NE8. The scattered points with dotted trend lines show the hybrid platform power downtimes. Solid lines show the reference case of power downtime for the wind turbine only case.

because the selection of the wave power threshold can change, it is important to evaluate the performance of the hybrid platform subject to different thresholds. Hence, in Fig. 13, we compute the power downtime in the three locations, VS, N3 and NE8 subject to different wave power thresholds. The horizontal axis of Fig. 13 shows the wave power threshold ranging from 0.1 MW to 10 MW. We recall that when wave power is equal or above the threshold, power production is considered available. Therefore, the hybrid wind and wave power downtimes, subject to different wave power threshold, are plotted for VS, N3 and NE8, with different markers as specified in the legend of Fig. 13. In Fig. 13, dotted lines are used to interpolate the markers. The same colour code is used for the three different locations, as the one used in the previous section. For comparison, Fig. 13 also shows the power downtime due to wind only for the three locations, VS, N3 and NE8, as flat horizontal lines, showing 7.4 %, 4.7 % and 5.4 % downtime, respectively.

Fig. 13 shows that reduction in power downtime is still feasible up to 2 MW in VS and N3. For example, considering a 1 MW threshold, we recall that power downtime drops by approximately 43 % in VS and 36 % in N3. Considering a 2 MW threshold, these numbers change to 19 % and 17 %, respectively. Furthermore, the red dotted line in Fig. 13 reveals that over the range of 0.3 MW to 2 MW wave power threshold, a steep drop in power is achieved in VS. In contrast, the blue dotted line shows that for N3, a more gradual and uniform drop in power is obtained over the same wave power threshold range. The black dotted line shows that for NE8, a gradual and less steep drop in power occurs, extending from 100 kW to approximately 1 MW.

As the wave power threshold increases to 3 MW in VS and N3, and to 1 MW in NE8, the hybrid power downtime curves asymptote to similar downtime levels where only wind power is considered, i.e. the baseline cases. Therefore, the sensitivity analysis shown in Fig. 13 confirms that the performance of the hybrid platform is superior in high wave power density locations with low to intermediate correlation. However, the hybrid platform can also perform satisfactorily in low wave power density and high correlation locations, provided that the wave power threshold is relaxed to lower thresholds. In the case of Fig. 13, to thresholds below 1 MW.

6. Discussion

The results obtained in this work highlight that a hybrid wind wave platform is functional for applications where a minimum power baseload is required. For example, the case of PEM electrolysers, which are designed to operate in steady state, and cycles of on and off switching are preventable if at least 20 % of their power rating is provided. Considering the case of the hybrid platform and a 5 MW wind turbine, then a minimum baseload of 1 MW would be required to keep a 5 MW electrolyser continuously running (Niblett et al., 2024).

The sensitivity analysis carried out in the previous section showed that the hybrid platform can reduce effectively the power downtime over a range of wave power thresholds and up to 2 MW in high wave energy density and low to intermediate wind-wave correlation locations. However, it is important to mention that the wave energy conversion system of the hybrid platform can be improved through hull geometry or parallel arrays of platforms. As such, the disparity between wave and wind power can be reduced. Furthermore, the smoothness of the power output can be increased, by reducing the scale of the wind turbine. Hence, the design of the hybrid platform can be modified according to different performance objectives.

An important consideration for performance of wind wave hybrid platforms is the metocean properties of the selected site. High wave power density with low correlation sites are locations where the hybrid platform shows the highest drop in wind downtime power. This is because wave power is more available due to the high energy contained in swell waves. Additionally, the complementary of wind and wave resources is highest in low correlation sites. In contrast, although the hybrid platform can also provide power downtime reduction in high correlation sites, the fact that wave power density is typically lower due to enclosed basins surrounded by land masses, signifies a slight reduction in performance of the hybrid platform. Hence, ideally, hybrid wind wave platforms are suitable for open sea swell dominated locations, where wind and wave resource have low to intermediate correlation indices ($C \leq 0.7$).

Lastly, note that the selection of wave power as the principal complement of wind energy over other sources of renewable energy, such as solar energy, is preferred due to a reduced footprint in surface area requirements. This is important because firstly, a lower surface area footprint reduces manufacturing costs, and secondly, it allows scalability with platforms in parallel.

7. Conclusions

This paper develops the novel concept of a hybrid wind and wave floating platform to provide a minimum power base load for offshore applications. Different to alternative hybrid wind-wave platforms and wind and wave complementarity studies, in this work, we proposed a novel hinged-connected hybrid platform, which is modular and scalable, in order to provide a minimum power baseload. By considering the case of offshore PEM electrolysers, whose operational life is reduced when the power baseload drops below 20 % of their rated capacity (Niblett et al., 2024), wave power reduces the downtime in which the PEM electrolyser would have to be shut down in only wind power was available.

The platform is built with three pontoons that are interconnected with two hinges. A 5 MW wind turbine is mounted on deck. The influence of the wind turbine in the motion of the platform is not detrimental to hinge motion performance, since hydrodynamic loading is the dominant factor that determines the motion of the platform.

The wind turbine is installed downstream of the platform where platform motions are controlled through two mechanisms. One is the passive reduction of pitching motions through more energy absorption of the upstream hinge. The second one is active, through setting the PTO damping to operate in optimum power conditions. A numerical model was developed to compute wave power for the hybrid platform through hinge motion. Due to reduced pitch motions downstream of the floating platform and control capabilities of the wind turbine, the power curve of the 5 MW wind turbine is considered.

In order to assess the performance of the hybrid platform to reduce wind power downtime and to supply a minimum power baseload, three different locations are considered: One off the coast of Spain (VS), and two off the coast of Scotland, one on the west coast (N3) and one in the North Sea (NE8). The sites were selected to evaluate the hybrid platform subject to low, intermediate and high wind wave correlation indices, respectively. In terms of power performance of the platform we found that:

- Wave power production of the platform is broadband due to the presence of the two hinges, and is highest between $10\,s \leq T_s \leq 14\,s$, which is a region of significant wave power in multiple locations of the world (Arredondo-Galeana et al., 2023b, 2024). Naturally, wave power increases also with wave height.
- Long term metocean data analysis of 20 years (2000–2019) revealed that wind power downtime is inversely proportional to wind power density, and that the ability of the platform to provide a minimum power base load relies on two factors: Firstly, high wave power density. Secondly, low to intermediate wind and wave correlation index. Hence, swell dominated regions with low wind and wave correlation indices are ideal for this type of hybrid platform.
- Assuming that $\text{downtime} = \text{wave power} < 1$ MW and considering three locations with different metocean properties (VS, N3 and NE8), our analysis showed that the hybrid platform decreases wind power downtime the most in VS and N3, by up to 43 % and 36 %, respectively. This is approximately equivalent to a reduction of 5500 and

3000 downtime hours in a window of 20 years, in VS and N3, respectively.
- Sensitivity analysis shows that wave power thresholds of up to 2 MW can provide a significant reduction in wind power downtime in VS and N3. In NE8, power downtime could be achieved by lowering the wave power threshold to the kW range.

In summary, the hybrid wind and wave platform presented in this work is able to provide a minimum power threshold for offshore applications that suffer from periods of time where wind power is absent, and that require a minimum level of power for continuous operation. The design of the hybrid platform is scalable, and can be tailored to meet other requirements, making the current design a versatile concept worth of further development and investigation.

Further avenues of research include 1) Improving pontoon design to prevent water slamming and water on deck due to low freeboard, 2) Performing a time-domain analysis to understand the effects of transient wind and wave loading on fatigue life and power performance of the hybrid platform, 3) Expanding the numerical model to account for mooring line forces and viscous losses, 4) Optimising pontoon geometry for wave power capture and 5) Assessing passive yaw capabilities of the platform.

Data available statement

The experimental data supporting the findings of this study were acquired at the Kelvin Hydrodynamics Laboratory at the University of Strathclyde using a hinged, connected prototype VLFS. The data are openly available in the Zenodo repository at https://doi.org/10.5281/zenodo.10067451.

CRediT authorship contribution statement

Abel Arredondo-Galeana: Writing – review & editing, Writing – original draft, Validation, Software, Methodology, Investigation, Formal analysis, Data curation, Conceptualization; **Gabriel Thomas Scarlett:** Writing – review & editing, Methodology, Investigation, Formal analysis; **Maurizio Collu:** Supervision, Project administration, Methodology, Investigation, Funding acquisition, Conceptualization; **Feargal Brennan:** Supervision, Project administration, Methodology, Investigation, Funding acquisition, Conceptualization.

Declaration of competing interest

The authors declare that they have no known competing financial interests or personal relationships that could have appeared to influence the work reported in this paper.

Acknowledgments

This work was funded by the UK Engineering and Physical Sciences Research Council (EPSRC) as part of the Ocean-REFuel (Ocean Renewable Energy Fuels) Programme Grant EP/W005212/1 awarded to the University of Strathclyde, Newcastle University, University of Nottingham, Cardiff University and Imperial College London. This work also received funding as part of the Supergen ORE Impact Hub 2023 Programme Grant EP/Y016297/1 and Early Career Research Grant “ECRRF2023 - (Call 6) -11” from the Supergen ORE Impact Hub 2023. The first author would like acknowledge Yongqiang Chen from Shanghai Jiao Tong University for providing the hydrodynamic coefficients utilised to compute the dynamic response of the hinged VLFS.

Supplementary material

Supplementary material associated with this article can be found, in the online version, at 10.1016/j.oceaneng.2025.123090

References

Aboutalebi, P., Garrido, A.J., Garrido, I., Nguyen, D.T., Gao, Z., 2024. Hydrostatic stability and hydrodynamics of a floating wind turbine platform integrated with oscillating water columns: a design study. Renew. Energy 221, 119824. https://doi.org/10.1016/j.renene.2023.119824

Allen, C., Viscelli, A., Dagher, H., Goupee, A., Gaertner, E., Abbas, N., Hall, M., Barter, G., 2020. Definition of the UMaine VolturnUS-S reference platform developed for the IEA wind 15-megawatt offshore reference wind turbine. Technical Report. National Renewable Energy Lab.(NREL), Golden, CO (United States); Univ. of ...

ARREDONDO-GALEANA, A., 2023. Rigid and hinged very large floating structure (VLFS) dataset - kelvin hydrodynamics laboratory. https://doi.org/10.5281/zenodo.10067451

Arredondo-Galeana, A., Brennan, F., 2021. Floating offshore vertical axis wind turbines: opportunities, challenges and way forward. Energies 14 (23). https://doi.org/10.3390/en14238000

Arredondo-Galeana, A., Dai, S., Chen, Y., Zhang, X., Brennan, F., 2023a. Understanding the force motion trade off of rigid and hinged floating platforms for marine renewables. Proceed. Eur. Wave Tidal Energy Conferen. 15. https://doi.org/10.36688/ewtec-2023-389

Arredondo-Galeana, A., Ermakov, A., Shi, W., Ringwood, J.V., Brennan, F., 2024. Optimal control of wave cycloidal rotors with passively morphing foils: an analytical and numerical study. Mar. Struct. 95, 103597. https://doi.org/10.1016/j.marstruc.2024.103597

Arredondo-Galeana, A., Olbert, G., Shi, W., Brennan, F., 2023b. Near wake hydrodynamics and structural design of a single foil cycloidal rotor in regular waves. Renew. Energy 206, 1020–1035. https://doi.org/10.1016/j.renene.2023.02.068

Astariz, S., Iglesias, G., 2016. Selecting optimum locations for co-located wave and wind energy farms. part I: the co-location feasibility index. Energy Convers. Manage. 122, 589–598. https://doi.org/10.1016/j.enconman.2016.05.079

Astariz, S., Iglesias, G., 2017. The collocation feasibility index - a method for selecting sites for co-located wave and wind farms. Renew. Energy 103, 811–824. https://doi.org/10.1016/j.renene.2016.11.014

Astariz, S., Vazquez, A., Sánchez, M., Carballo, R., Iglesias, G., 2018. Co-located wave-wind farms for improved o&m efficiency. Ocean Coast. Manage. 163, 66–71. https://doi.org/10.1016/j.ocecoaman.2018.04.010

Borg, M., Collu, M., Brennan, F.P., 2013. Use of a wave energy converter as a motion suppression device for floating wind turbines. Energy Proced. 35, 223–233. DeepWind’2013 - Selected papers from 10th Deep Sea Offshore Wind R&D Conference, Trondheim, Norway, 24 - 25 January 2013. https://doi.org/10.1016/j.egypro.2013.07.175

Celesti, M.L., Paduano, B., Peña-Sanchez, Y., Pasta, E., Faedo, N., Ringwood, J.V., 2023. On the behaviour of a combined wind-wave energy conversion platform under energy-maximising control conditions. In: OCEANS 2023-Limerick. IEEE, pp. 1–6.

Chen, D., Feng, X., Li, Z., Chen, J.-F., 2023. Long-term extreme responses of torsional moments at two-directional hinges for moored very large floating structures. Ocean Eng. 290, 116330. https://doi.org/10.1016/j.oceaneng.2023.116330

DNV, 2007. Recommended Practice DNV-RP-C205. Environmental conditions and environmental loads. Det Norske Veritas, Høvik, Norway.

Dong, X., Li, Y., Li, D., Cao, F., Jiang, X., Shi, H., 2022. A state-of-the-art review of the hybrid wind-wave energy converter. Progr. Energy 4 (4), 042004. https://doi.org/10.1088/2516-1083/ac821d

Edwards, E.C., Holcombe, A., Brown, S., Ransley, E., Hann, M., Greaves, D., 2023. Evolution of floating offshore wind platforms: a review of at-sea devices. Renew. Sustain. Energy Rev. 183, 113416. https://doi.org/10.1016/j.rser.2023.113416

Flex2Future, Flex2Future. Game-Changing Offshore Energy Solutions. https://flex2future.com/. Accessed: 2025-06-15.

Folley, M., Whittaker, T., 2010. Spectral modelling of wave energy converters. Coast. Eng. 57 (10), 892–897. https://doi.org/10.1016/j.coastaleng.2010.05.007

Fusco, F., Nolan, G., Ringwood, J.V., 2010. Variability reduction through optimal combination of wind/wave resources - an irish case study. Energy 35 (1), 314–325. https://doi.org/10.1016/j.energy.2009.09.023

Gao, Q., Khan, S.S., Sergiienko, N., Ertugrul, N., Hemer, M., Negnevitsky, M., Ding, B., 2022. Assessment of wind and wave power characteristic and potential for hybrid exploration in australia. Renew. Sustain. Energy Rev. 168, 112747. https://doi.org/10.1016/j.rser.2022.112747

Gaspar, J.F., Kamarlouei, M., Thiebaut, F., Guedes Soares, C., 2021. Compensation of a hybrid platform dynamics using wave energy converters in different sea state conditions. Renew. Energy 177, 871–883. https://doi.org/10.1016/j.renene.2021.05.096

Ghafari, H.R., Ghassemi, H., He, G., 2021. Numerical study of the wavestar wave energy converter with multi-point-absorber around deepcwind semisubmersible floating platform. Ocean Eng. 232, 109177. https://doi.org/10.1016/j.oceaneng.2021.109177

Gubesch, E., Sergiienko, N.Y., Nader, J.-R., Ding, B., Cazzolato, B., Penesis, I., Li, Y., 2023. Experimental investigation of a co-located wind and wave energy system in regular waves. Renew. Energy 219, 119520. https://doi.org/10.1016/j.renene.2023.119520

Guo, B., Ringwood, J.V., 2021. A review of wave energy technology from a research and commercial perspective. IET Renew. Power Gener. 15 (14), 3065–3090. https://doi.org/10.1049/rpg2.12302

Hallak, T.S., Guedes Soares, C., 2025. Overview of the recent developments in hybrid floating wind-wave platforms. J. Mar. Sci. Appl. 24 (1), 98–119. https://doi.org/10.1007/s11804-024-00544-w

Hosseinzadeh, S., Stewart, R.A., Kamranzad, B., Etemad-Shahidi, A., 2025. Evaluation of australian offshore wind and wave energy resources for joint exploitation. Ocean Eng. 328, 121066. https://doi.org/10.1016/j.oceaneng.2025.121066

Ioannou, A., Liang, Y., Jalón, M.L., Brennan, F.P., 2020. A preliminary parametric techno-economic study of offshore wind floater concepts. Ocean Eng. 197, 106937. https://doi.org/10.1016/j.oceaneng.2020.106937

Jin, S., Greaves, D., 2021. Wave energy in the UK: status review and future perspectives. Renew. Sustain. Energy Rev. 143, 110932. https://doi.org/10.1016/j.rser.2021.110932

Jonkman, J., Butterfield, S., Musial, W., Scott, G., 2009. Definition of a 5-MW reference wind turbine for offshore system development. Technical Report. National Renewable Energy Lab.(NREL), Golden, CO (United States).

Jonkman, J.M., Buhl, , M.L. Jr, 2007. Loads analysis of a floating offshore wind turbine using fully coupled simulation: preprint. United States. Contract Number: AC36-99-GO10337. https://www.osti.gov/biblio/909454.

Kalogeri, C., Galanis, G., Spyrou, C., Diamantis, D., Baladima, F., Koukoula, M., Kallos, G., 2017. Assessing the european offshore wind and wave energy resource for combined exploitation. Renew. Energy 101, 244–264. https://doi.org/10.1016/j.renene.2016.08.010

LAUTEX, E., Available at: https://esox.lautec.com/map/. Accessed: 2023-10-25.

McNatt, J.C., Retzler, C.H., 2020. The performance of the mocean m100 wave energy converter described through numerical and physical modelling. Int. Marin. Energy J. 3 (1), 11–19. https://doi.org/10.36688/imej.3.11-19

Mei, C.C., Newman, J.N., 1980. Wave power extraction by floating bodies. In: 1st Symposium on Wave Energy Utilisation.

Niblett, D., Delpisheh, M., Ramakrishnan, S., Mamlouk, M., 2024. Review of next generation hydrogen production from offshore wind using water electrolysis. J. Power Source. 592, 233904. https://doi.org/10.1016/j.jpowsour.2023.233904

Noad, I.F., Porter, R., 2017a. Approximations to wave energy absorption by articulated rafts. SIAM J. Appl. Math. 77 (6), 2199–2223. https://doi.org/10.1137/16M1104743

Noad, I.F., Porter, R., 2017b. Modelling an articulated raft wave energy converter. Renew. Energy 114, 1146–1159. https://doi.org/10.1016/j.renene.2017.07.077

Papi, F., Bianchini, A., 2022. Technical challenges in floating offshore wind turbine upscaling: a critical analysis based on the NREL 5 MW and IEA 15 MW reference turbines. Renew. Sustain. Energy Rev. 162, 112489. https://doi.org/10.1016/j.rser.2022.112489

Pennock, S., Noble, D.R., Vardanyan, Y., Delahaye, T., Jeffrey, H., 2023. A modelling framework to quantify the power system benefits from ocean energy deployments. Appl. Energy 347, 121413. https://doi.org/10.1016/j.apenergy.2023.121413

Pérez-Collazo, C., Greaves, D., Iglesias, G., 2015. A review of combined wave and offshore wind energy. Renew. Sustain. Energy Rev. 42, 141–153. https://doi.org/10.1016/j.rser.2014.09.032

Reikard, G., Robertson, B., Bidlot, J.-R., 2015. Combining wave energy with wind and solar: short-term forecasting. Renew. Energy 81, 442–456. https://doi.org/10.1016/j.renene.2015.03.032

Rodríguez Castillo, C.A., Collu, M., Brennan, F., 2025. Comparative design space exploration of centred and off-centred semisubmersible configurations for floating offshore wind turbines. Ocean Eng. 324, 120740. https://doi.org/10.1016/j.oceaneng.2025.120740

Rusu, L., Onea, F., 2017. The performance of some state-of-the-art wave energy converters in locations with the worldwide highest wave power. Renew. Sustain. Energy Rev. 75, 1348–1362. https://doi.org/10.1016/j.rser.2016.11.123

Said, H.A., Costello, S., Ringwood, J., 2023. On the complementarity of wave, tidal, wind and solar resources in ireland. In: Proceedings of the European Wave and Tidal Energy Conference. Vol. 15. European Wave and Tidal Energy Conference EWTEC, pp. 1–6. https://doi.org/10.36688/ewtec-2023-340

Scarlett, G.T., McNatt, J.C., Henry, A., Arredondo-Galeana, A., 2024. Energy flux method for wave energy converters. Energies 17 (19). https://doi.org/10.3390/en17194991

Stansby, P., Li, G., 2024. A wind semi-sub platform with hinged floats for omnidirectional swell wave energy conversion. J. Ocean Eng. Marin. Energy 10 (2), 433–448. https://doi.org/10.1007/s40722-024-00321-5

Tay, Z.Y., 2019. Energy extraction from an articulated plate anti-motion device of a very large floating structure under irregular waves. Renew. Energy 130, 206–222. https://doi.org/10.1016/j.renene.2018.06.044

Thomassen, P.E., Bruheim, P.I., Suja, L., Frøyd, L., 2012. A novel tool for FEM analysis of offshore wind turbines with innovative visualization techniques. Vol. All Days of *International Ocean and Polar Engineering Conference*, pp. ISOPE–I–12–080.

Tran, T.-T., Kim, D.-H., 2015. The platform pitching motion of floating offshore wind turbine: a preliminary unsteady aerodynamic analysis. J. Wind Eng. Ind. Aerodyn. 142, 65–81. https://doi.org/10.1016/j.jweia.2015.03.009

Veers, P., Dykes, K., Lantz, E., Barth, S., Bottasso, C.L., Carlson, O., Clifton, A., Green, J., Green, P., Holttinen, H., Laird, D., Lehtomäki, V., Lundquist, J.K., Manwell, J., Marquis, M., Meneveau, C., Moriarty, P., Munduate, X., Muskulus, M., Naughton, J., Pao, L., Paquette, J., Peinke, J., Robertson, A., Rodrigo, J.S., Sempreviva, A.M., Smith, J.C., Tuohy, A., Wiser, R., 2019. Grand challenges in the science of wind energy. Science 366 (6464), eaau2027. https://doi.org/10.1126/science.aau2027

Wan, L., Moan, T., Gao, Z., Shi, W., 2024. A review on the technical development of combined wind and wave energy conversion systems. Energy 294, 130885. https://doi.org/10.1016/j.energy.2024.130885

Wang, M., BaoX., Qu, M., Wang, T., Iglesias, G., 2025. Power performance and motion characteristics of a floating hybrid wind-wave energy system. Ocean Eng. 318, 120184. https://doi.org/10.1016/j.oceaneng.2024.120184

Wen, B., Dong, X., Tian, X., Peng, Z., Zhang, W., Wei, K., 2018. The power performance of an offshore floating wind turbine in platform pitching motion. Energy 154, 508–521. https://doi.org/10.1016/j.energy.2018.04.140

Yde, A., Pedersen, M., Bellew, S., Køhler, A., Clausen, R., Wedel Nielsen, A., 2014. Experimental and Theoretical Analysis of a Combined Floating Wave and Wind Energy Conversion Platform. Number 0044 In DTU Wind Energy E, DTU Wind Energy, Denmark.

Zhang, D., Du, J., Yuan, Z., Yu, S., Li, H., 2023a. Motion characteristics of large arrays of modularized floating bodies with hinge connections. Phys. Fluid. 35 (7), 077107. https://doi.org/10.1063/5.0153317

Zhang, J., Zhao, X., Greaves, D., Jin, S., 2023b. Modeling of a hinged-raft wave energy converter via deep operator learning and wave tank experiments. Appl. Energy 341, 121072. https://doi.org/10.1016/j.apenergy.2023.121072

Zhang, X., Lu, D., Guo, F., Gao, Y., Sun, Y., 2018. The maximum wave energy conversion by two interconnected floaters: effects of structural flexibility. Appl. Ocean Res. 71, 34–47. https://doi.org/10.1016/j.apor.2017.12.003

Zhang, X., Lu, D., Liang, Y., Brennan, F., 2021. Feasibility of very large floating structure as offshore wind foundation: effects of hinge numbers on wave loads and induced responses. J. Waterw., Port, Coast. Ocean Eng. 147 (3), 04021002. https://doi.org/10.1061/(ASCE)WW.1943-5460.0000626

Zhou, B., Hu, J., Zhang, Q., Wang, L., Jing, F., Collu, M., 2023. Optimal design and performance analysis of a hybrid system combining a semi-submersible wind platform and point absorbers. J. Mar. Sci. Eng. 11 (6). https://doi.org/10.3390/jmse11061190